Journal of Power Sources 204 (2012) 205–212

Contents lists available at SciVerse ScienceDirect

Journal of Power Sources

journal homepage: www.elsevier.com/locate/jpowsour

Studies of copper as a modifier in C14-predominant AB_2 metal hydride alloys

K. Young*, T. Ouchi, B. Huang, B. Reichman, M.A. Fetcenko

Energy Conversion Devices Inc./Ovonic Battery Company, 2983 Waterview Drive, Rochester Hills, MI 48309, USA

ARTICLE INFO

Article history:
Received 18 November 2011
Received in revised form
26 December 2011
Accepted 1 January 2012
Available online 9 January 2012

Keywords:
Hydrogen absorbing materials
Transition metal alloys
Metal hydride electrode
Electrochemical reactions

ABSTRACT

The structure, gaseous storage, and electrochemical properties of Cu-modified C14-predominant AB_2 metal hydride alloys with compositions of $Ti_{12}Zr_{21.5}V_{10}Cr_{7.5}Mn_{8.1}Co_{8.0-x}Ni_{32.2}Cu_xSn_{0.3}Al_{0.4}$, $x = 0$ to 5 were studied. As the Cu-content in the alloy increases, the lattice constant a increases (except at the highest Cu-content); both the lattice constants a, c, and the volume of the C14 unit cell increase; a/c ratio decreases; and the secondary phase shifts from a combination of C15 and TiNi to Zr_7Ni_{10}. In the gaseous phase reaction (analyzed by the pressure–concentration–temperature isotherm), the plateau pressure decreases; both the slope factor and hysteresis increase; and both the maximum and reversible hydrogen capacities decrease with the addition of Cu. Calculations of the heat of formation and the change in entropy indicate incompleteness of an ordered metal hydride structure. While the secondary phase plays a more important role in the gaseous reaction, the main phase determines the electrochemical properties. With the addition of Cu, both the high-rate and full discharge capacities increase; however, the ratio between the two capacities decreases due to lower bulk diffusibility of hydrogen, and activation becomes easier due to a higher pulverization rate. A good tradeoff between surface area and charge-transfer resistance, 1 at.% Cu-addition is recommended for the low-temperature application of C14-predominant AB_2 alloys.

1. Introduction

Due to the recent dramatic price increase of rare-earth metals, transition metal-based AB_2 alloys have become desirable for nickel/metal hydride (Ni/MH) manufactures to replace AB_5 alloys (currently used as the active material in the negative electrode) with. The multi-component nature of AB_2 alloys allows the incorporation of other modifying elements to optimize various electrochemical properties [1–3]. Among these modifiers is Cu, a very inexpensive element used in AB_5 alloys to improve the low-temperature characteristic by modifying the surface oxide structure and the metallic clusters imbedded into the bulk [4–6]. It is important to verify that Cu contributes to the low-temperature performance of AB_2 metal hydride (MH) alloys as well.

Studies of Cu as a modifier for AB_2 alloys have been previously conducted. In the gaseous phase reaction, Cu in the $ZrCr_2$, $TiCr_2$, and $TiMn_2$-based alloys increases the equilibrium plateau pressures and decreases storage capacities [7–10]. Cu in an annealed TiZrCrMn alloy flattens the isotherm and reduces the hysteresis in the pressure–concentration–temperature (PCT) measurement [11]. In electrochemical studies, Cu in the multi-element AB_2 alloys degrades the capacity [12,13] and deteriorates the cycle stability [14]. Besides alloying, Cu powder was also used as an additive in the negative electrode to suppress the cell pressure, increase the discharge capacity, and improve the cycle life [15–17]. These earlier Cu studies were performed either in the basic alloy system or alloys without optimization and did not include any mention of the changes in structure or the role of secondary phases. Therefore, a systematic investigation of Cu in the modern AB_2 MH alloys that are suitable for general Ni/MH battery application is needed and presented in this paper.

2. Experimental setup

Arc melting was performed under a continuous argon flow with a non-consumable tungsten electrode and a water-cooled copper tray. Before each run, a piece of sacrificial titanium underwent a melting-cooling cycle a few times to reduce the residual oxygen concentration. Each 12-g ingot was re-melted and turned over a few times to ensure uniformity in chemical composition. The chemical composition of each sample was examined by a Varian *Liberty* 100 inductively coupled plasma (ICP) system. A Philips *X'Pert Pro* X-ray diffractometer (XRD) was used to study the micro-structure, and a JOEL-*JSM6320F* scanning electron microscopy (SEM) with energy dispersive spectroscopy (EDS) capability was used to study the phase distribution and composition. PCT characteristics for each sample were measured using a Suzuki-Shokan multi-channel PCT system. In the PCT analysis, each sample was first activated by a

* Corresponding author. Tel.: +1 248 293 7000; fax: +1 248 299 4520.
E-mail address: kwoyoung@yahoo.com (K. Young).

0378-7753/$ – see front matter © 2012 Elsevier B.V. All rights reserved.
doi:10.1016/j.jpowsour.2012.01.030

2 h thermal cycle between 300 °C and room temperature at 25 atm H_2 pressure. The PCT isotherms at 30 °C and 60 °C were then measured. Details of both electrode and cell preparations as well as measurement methods have been reported previously [18,19]. AC impedance measurements were conducted using a Solartron 1250 Frequency Response Analyzer with sine waves of amplitude 10 mV and frequency range of 10 mHz to 10 kHz. Prior to the measurements, the electrodes were subjected to one full charge/discharge cycle at 0.1 C rate using a Solartron 1470 Cell Test galvanostat, discharged to 80% state-of-charge, and then cooled to −40 °C.

3. Results and discussion

Six alloys with Cu substituting for Co at various levels from 0 to 5 at.% ($Ti_{12}Zr_{21.5}V_{10}Cr_{7.5}Mn_{8.1}Co_{8.0-x}Ni_{32.2}Cu_xSn_{0.3}Al_{0.4}$, $x = 0$ to 5) were prepared, and the design compositions are listed in Table 1. The base alloy (Cu0) was selected due to its good high-rate dischargeability (HRD) and has also been used in the studies of effects of Fe [20] and Mo [21] modifiers on structural, hydrogen storage, and electrochemical properties. The average electron density (e/a) for each alloy, calculated from the numbers of outer-shell electrons of the constituent elements, is listed in Table 1. These e/a values are lower than the C14/C15 threshold of 7.0–7.1, and therefore a C14-predominant structure is predicted [22,23]. The designed stoichiometric ratio (B/A) is very close to 2.0. The ICP results, shown in the same table, are close to the target values except for small Cr-inhomogeneities present in the arc-melted samples. The calculated e/a values and B/A ratio based on the ICP results are very close to the designed values.

3.1. XRD structure analysis

The XRD patterns of the six alloys are shown in Fig. 1. All the major peaks can be fit into a hexagonal C14 ($MgZn_2$) structure. In Cu0, Cu1, and Cu2, the peak at around 41.5° corresponds to a B2-structured TiNi secondary phase [24]. This phase is the precursor of further solid-state transformation into Zr_xNi_y type of secondary phases [25,26]. In samples with higher concentrations of Cu, reflections from Zr_7Ni_{10} can also be observed.

The lattice constants of C14 structure, a and c (calculated from the XRD patterns) are listed in Table 2 and plotted in Fig. 2. As the amount of Cu increases, both a and c increase due to the atomic radius of Cu being larger than that of the replaced Co (except for lattice constant a of Cu5). As Cu-content continues to increase, some Ni atoms may be pushed to the A-site, form dumbbell-shaped pairs, increase c, or decrease a as in the case of the AB_5 alloy [5]. The C14 unit cell volume (V_{C14}) of each alloy was calculated from the lattice constants; its values are listed in Table 2 and plotted in Fig. 2. As the Cu-content increases, V_{C14} increases monotonically and theoretically should facilitate the hydrogen absorption. The a/c aspect

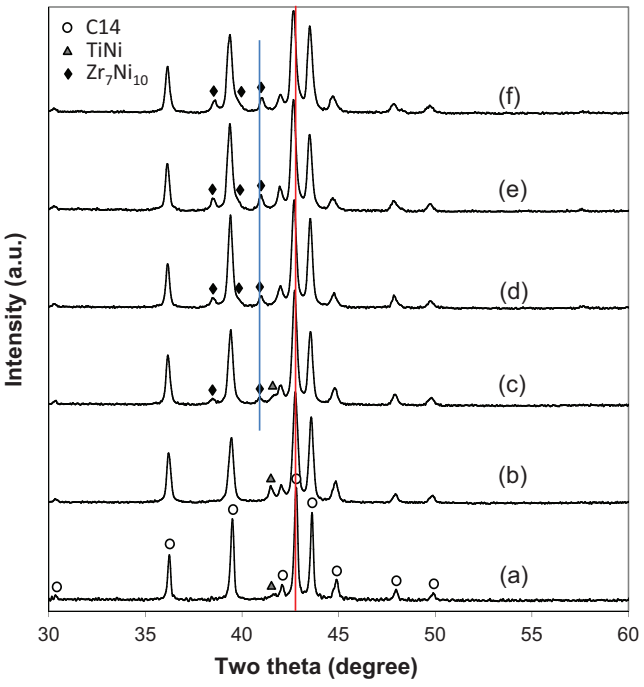

Fig. 1. XRD patterns using Cu Kα as the radiation source for alloys Cu0 (a), Cu1 (b), Cu2 (c), Cu3 (d), Cu4 (e), and Cu5 (f).

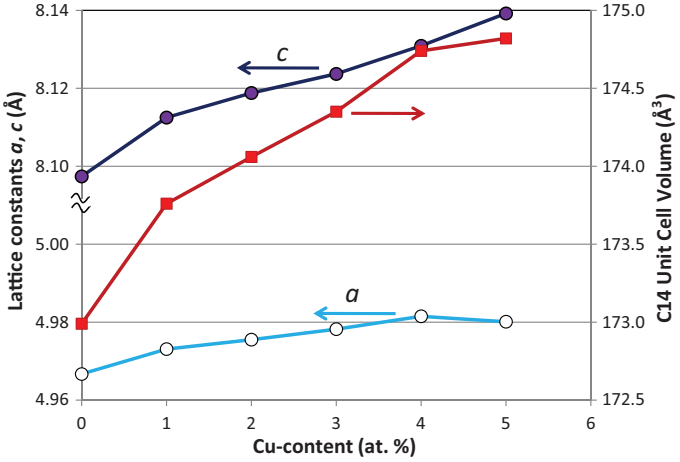

Fig. 2. Lattice constants and unit cell volume of the C14 main phase as functions of Cu-content.

Table 1
Designed compositions (in bold) and ICP results in at.%.

		Ti	Zr	V	Cr	Mn	Co	Ni	Cu	Sn	Al	e/a	B/A
Cu0	**Design**	**12.0**	**21.5**	**10.0**	**7.5**	**8.1**	**8.0**	**32.2**	**0.0**	**0.3**	**0.4**	**6.821**	**1.99**
	ICP	11.9	21.3	10.2	7.7	8.5	7.6	31.7	0.1	0.3	0.7	6.793	2.01
Cu1	**Design**	**12.0**	**21.5**	**10.0**	**7.5**	**8.1**	**7.0**	**32.2**	**1.0**	**0.3**	**0.4**	**6.841**	**1.99**
	ICP	12.4	21.3	9.7	6.9	7.9	6.9	33.2	1.0	0.3	0.4	6.875	1.97
Cu2	**Design**	**12.0**	**21.5**	**10.0**	**7.5**	**8.1**	**6.0**	**32.2**	**2.0**	**0.3**	**0.4**	**6.861**	**1.99**
	ICP	12.4	21.3	9.8	6.8	8.0	6.0	32.8	2.1	0.3	0.5	6.884	1.97
Cu3	**Design**	**12.0**	**21.5**	**10.0**	**7.5**	**8.1**	**5.0**	**32.2**	**3.0**	**0.3**	**0.4**	**6.881**	**1.99**
	ICP	12.4	21.5	9.9	6.8	8.0	5.0	32.6	3.1	0.3	0.4	6.894	1.95
Cu4	**Design**	**12.0**	**21.5**	**10.0**	**7.5**	**8.1**	**4.0**	**32.2**	**4.0**	**0.3**	**0.4**	**6.901**	**1.99**
	ICP	12.2	21.3	9.9	6.4	8.0	4.0	33.1	4.1	0.3	0.5	6.927	1.98
Cu5	**Design**	**12.0**	**21.5**	**10.0**	**7.5**	**8.1**	**3.0**	**32.2**	**5.0**	**0.3**	**0.4**	**6.921**	**1.99**
	ICP	12.1	21.5	9.6	7.8	8.0	2.9	32.4	4.9	0.3	0.5	6.919	1.98

Table 2
Lattice constants a and c, a/c ratios, C14 lattice volumes (V_{C14}), full widths at half maximum for (1 0 3) reflection peak, corresponding crystallite sizes, and phase abundances calculated from XRD analysis.

	a (Å)	c (Å)	a/c	V_{C14} (Å^3)	FWHM(103) (degree of 2θ)	Crystallite size (Å)	C14 phase abundance	C15 phase abundance	TiNi phase abundance	Zr_7Ni_{10} phase abundance
Cu0	4.9667	8.0974	0.6134	172.99	0.199	634	95.1%	3.1%	1.8%	ND
Cu1	4.9731	8.1125	0.6130	173.76	0.257	429	89.3%	8.1%	2.6%	ND
Cu2	4.9755	8.1188	0.6129	174.06	0.249	449	90.8%	6.1%	1.0%	2.1%
Cu3	4.9782	8.1237	0.6128	174.35	0.237	481	94.8%	ND	ND	5.2%
Cu4	4.9815	8.1309	0.6127	174.74	0.265	411	91.7%	1.1%	ND	7.2%
Cu5	4.9801	8.1392	0.6119	174.82	0.293	358	91.5%	ND	ND	7.7%

ratio decreases with increasing Cu-content and predicts a higher degree of pulverization during cycling [27–29].

The crystallite size of each alloy was estimated by the Scherrer equation [30] using the full-width at half maximum (FWHM) of the C14 (1 0 3) peak in the XRD pattern; its values are listed in Table 2. The crystallite sizes of the Cu-containing alloys are similar and smaller than that of the Cu-free alloy due to the increase in the density of Zr_7Ni_{10} secondary phase, a phenomenon which will be discussed in the next section.

The phase abundances analyzed by Jade 9 software are listed in Table 2. The software first identified and deconvoluted the peaks corresponding to the phases entered into the software. It then integrated the areas from peaks belong to the same phase. Phase abundances were obtained from these areas through previously established calibrations that used SEM/transmission electron microscope/ICP. In alloys Cu0, Cu1, and Cu2, the secondary phases are mainly C15 and TiNi while Zr_7Ni_{10} becomes the main secondary phase for the rest of the alloys with higher Cu-content. From an earlier study of the contributions of the phases to various properties in a series of AB_2 MH alloys, the TiNi phase was found to increase both the gaseous phase and electrochemical storage capacities, lower the hydrogen equilibrium pressure, and decrease the half-cell high-rate dischargeability (HRD), but Zr_7Ni_{10} had the opposite effects [24]. The current study provides a comparison of the secondary phase and the modifier in the main phase and their effects on structural, hydrogen storage, and electrochemical properties.

As stated previously, the dominating secondary phase in the alloys with relatively higher Cu-contents is Zr_7Ni_{10}. In a study of modifying the Zr_7Ni_{10} base alloy, Cu-substituted alloy retained the Zr_7Ni_{10} structure while others promoted C14 or C15 structures because Cu is the only element where Zr_7Cu_{10} is available as an intermetallic compound in the A_7B_{10} stoichiometry among the various modifying elements [31]. The lattice constants a, b, and c of the orthorhombic Zr_7Ni_{10} phases in alloys Cu2–Cu5 were calculated from the XRD patterns and are listed in Table 3 together with those from Zr_7Ni_{10} and Zr_7Cu_{10}. The trends of changes in a and b are not clear; therefore, a nontraditional approach is taken to describe the crystal structure. Zr_7Ni_{10} has an orthorhombic crystal structure where $a \neq b \neq c$ and $\alpha = \beta = \gamma = 90^\circ$. As shown in Fig. 3, the rectangular base can be related to a rhombus with a side length of half of its diagonal ($d/2$) and an internal angle $\theta \neq 90^\circ$. The calculated values for $d/2$ and θ are listed in Table 3. As the Cu-content increases, the $d/2$ value decreases; the rhombus becomes closer to a square (tetragonal structure, another structure reported for Zr_7Ni_{10} after hydrogenation [32–34]); and the unit cell of Zr_7Ni_{10} phase shrinks. The change in Zr_7Ni_{10} phase unit cell volume is in the opposite direction to that in the main C14 phase unit cell volume, which can also be seen from the XRD patterns in Fig. 1: as the Cu-content increases, the marked C14 peak moves to a lower angle while the Zr_7Ni_{10} peak moves to a higher angle. The reason for this discrepancy will be discussed in the SEM/EDS section.

Table 3
Lattice constants, half of the base diagonal, internal angle of the base rhombus, and orthorhombic lattice volume of the Zr_7Ni_{10} phase of alloys Cu2 to Cu5 calculated from XRD analysis. Data of Zr_7Ni_{10} and Zr_7Cu_{10} are presented for comparison purpose.

	a (Å)	b (Å)	c (Å)	$d/2$ (Å)	θ (°)	Unit cell vol. (Å^3)
Cu2	9.035	9.060	12.228	7.602	107.10	1000.9
Cu3	9.034	9.081	12.193	7.588	106.96	1000.3
Cu4	9.035	9.092	12.168	7.578	106.83	999.6
Cu5	9.071	9.073	12.138	7.577	106.48	999.0
Zr_7Ni_{10}	9.154	9.216	12.385	7.700	107.08	1044.8
Zr_7Cu_{10}	9.313	9.347	12.675	7.864	107.41	1103.3

3.2. SEM/EDS analysis

The microstructures for this series of alloys were studied by SEM, and the back-scattering electron images (BEI) are presented in Fig. 4. Samples were mounted and polished on epoxy blocks, rinsed and dried before entering the SEM chamber. The compositions in several areas (identified numerically in the micrographs) were studied by EDS, and the results are listed in Table 4. B/A ratios and e/a values calculated based on the compositions are listed in the same table. The base alloy Cu0 is mainly composed of AB_2 as the major phase (with B/A around 2.0) and TiNi (as identified from the XRD analysis) as the minor phase. The compositions of C14 and C15 phases are virtually the same and show no differentiable BEI contrasts. The e/a value of spot #1 is 7.04, which is right on the C14/C15 threshold and cannot be used to identify the phase structure. Occasional ZrO_2 inclusions are found in every sample of the current study. The Zr_7Ni_{10} phase (with the brightest BEI contrast due to its higher Zr-content) starts to appear once Cu is introduced in the alloy. As the Cu-content increases, it appears that the Zr_7Ni_{10} phase not only increases in size but also in abundance. Since the solubility of V in Zr_7Ni_{10} phase is very limited [35], higher Zr_7Ni_{10} abundance will push more V into the AB_2 main phase. When the V-content in the main phase increases to a certain amount, it will start to occupy the A-site and reduce the lattice size, as can be seen from the slowing-down in unit cell expansion at higher Cu substitution

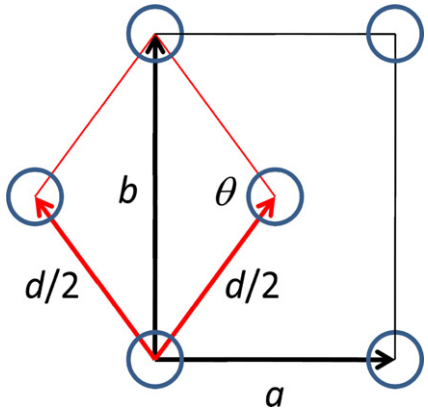

Fig. 3. Schematic diagram of the two different presentations of the a–b plane of Zr_7Ni_{10} structure.

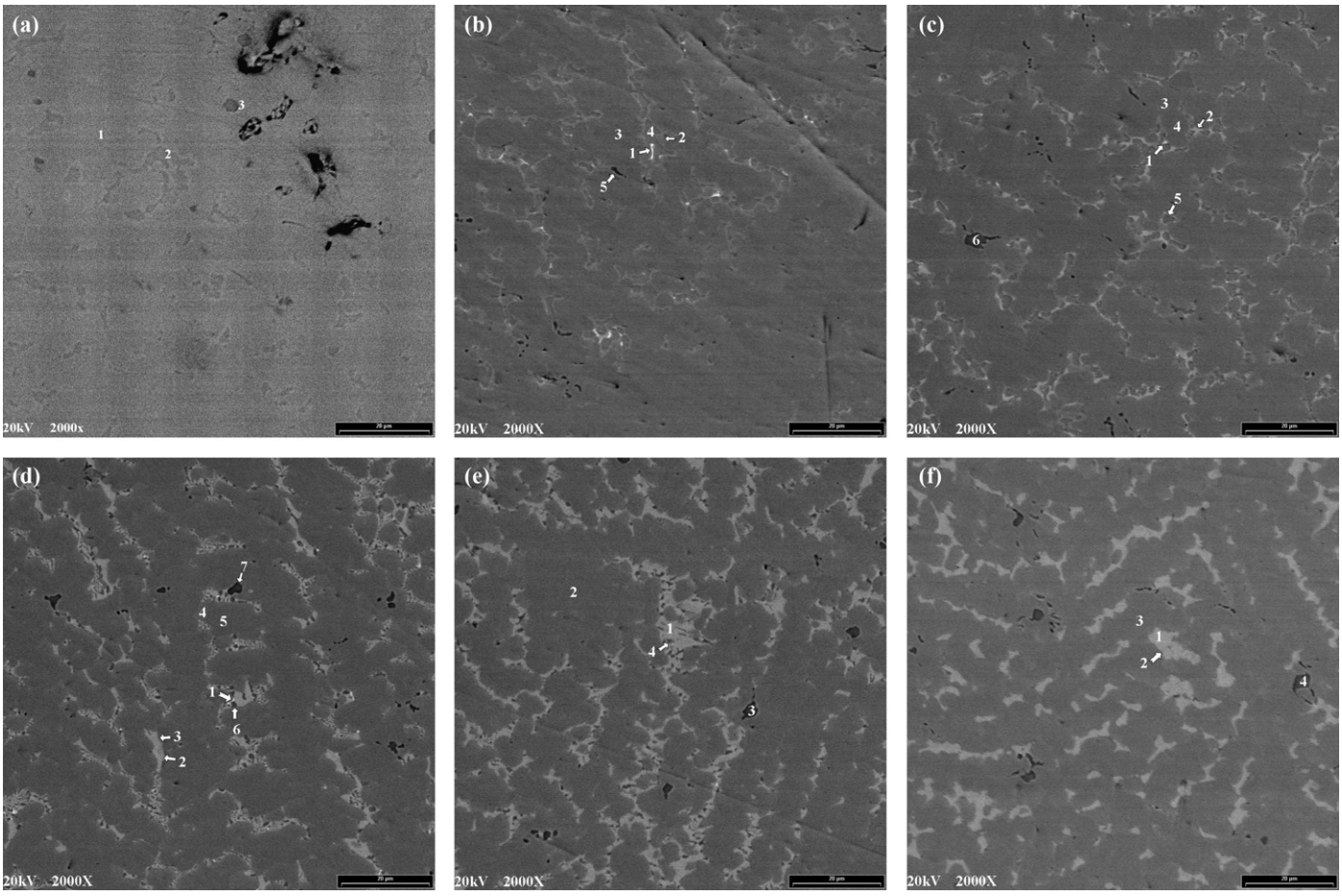

Fig. 4. SEM backscattering images for alloys Cu0 (a), Cu1 (b), Cu2 (c), Cu3 (d), Cu4 (e), and Cu5 (f).

Table 4
Summary of EDS results. All composition numbers are in atomic percentage. The main AB_2 phase is identified in bold.

	Ti	Zr	V	Ni	Co	Mn	Cr	Al	Cu	Sn	B/A	*e*/*a*	
Cu0-1	**14.6**	**19.4**	**8.6**	**38.3**	**6.4**	**7.5**	**5.1**	**0.0**	**0.0**	**0.1**	**1.94**	**7.04**	**AB_2**
Cu0-2	23.3	18.0	3.0	45.6	5.1	3.5	1.4	0.0	0.0	0.1	1.42	7.16	TiNi
Cu0-3	3.9	80.4	3.4	6.2	1.3	2.1	2.2	0.0	0.0	0.5	0.19	4.63	ZrO_2
Cu1-1	16.4	24.8	1.4	42.3	2.2	2.3	0.5	0.2	2.6	7.3	1.43	7.65	Zr_7Ni_{10}
Cu1-2	16.0	20.4	5.7	42.2	4.8	5.3	2.9	0.4	1.7	0.6	1.75	7.22	AB_2/Zr_7Ni_{10}
Cu1-3	**10.6**	**19.9**	**12.6**	**29.3**	**7.6**	**9.7**	**9.4**	**0.4**	**0.5**	**0.1**	**2.28**	**6.79**	**AB_2**
Cu1-4	24.3	18.1	1.5	45.8	4.3	2.4	0.6	0.2	2.1	0.7	1.36	7.28	TiNi
Cu1-5	8.3	54.7	7.0	16.8	3.2	5.0	4.4	0.0	0.2	0.4	0.59	5.53	ZrO_2
Cu2-1	15.0	24.1	2.8	40.8	2.5	3.4	1.2	0.3	3.7	6.2	1.56	7.60	Zr_7Ni_{10}
Cu2-2	15.3	24.7	2.1	45.5	2.1	2.3	0.9	0.2	5.7	1.2	1.50	7.46	Zr_7Ni_{10}
Cu2-3	**11.9**	**20.3**	**11.7**	**32.0**	**6.1**	**9.1**	**7.2**	**0.3**	**1.2**	**0.2**	**2.11**	**6.86**	**AB_2**
Cu2-4	**10.7**	**20.3**	**12.6**	**29.5**	**6.5**	**9.9**	**9.4**	**0.0**	**1.0**	**0.1**	**2.23**	**6.79**	**AB_2**
Cu2-5	24.1	17.2	1.5	45.7	4.0	2.9	0.5	0.2	3.2	0.7	1.42	7.35	TiNi
Cu2-6	2.1	88.7	1.7	4.0	0.4	1.1	1.0	0.5	0.1	0.5	0.10	4.39	ZrO_2
Cu3-1	14.1	23.9	2.8	41.4	1.9	3.8	0.9	0.3	6.1	4.8	1.63	7.64	Zr_7Ni_{10}
Cu3-2	15.5	23.9	0.8	48.7	1.6	1.2	0.2	0.2	7.2	0.7	1.54	7.62	Zr_7Ni_{10}
Cu3-3	15.7	23.0	0.8	48.9	1.6	1.3	0.3	0.0	7.8	0.7	1.59	7.69	Zr_7Ni_{10}
Cu3-4	**10.7**	**21.9**	**12.9**	**28.6**	**5.6**	**10.0**	**8.2**	**0.5**	**1.3**	**0.1**	**2.06**	**6.68**	**AB_2**
Cu3-5	**9.8**	**20.4**	**13.1**	**27.9**	**5.9**	**11.1**	**10.4**	**0.3**	**1.0**	**0.2**	**2.31**	**6.71**	**AB_2**
Cu3-6	25.7	13.2	1.8	44.5	4.2	3.9	0.6	0.2	5.0	0.8	1.57	7.45	TiNi
Cu3-7	1.9	91.5	1.2	2.7	0.2	0.6	0.7	0.3	0.1	0.7	0.07	4.29	ZrO_2
Cu4-1	15.8	22.1	1.6	46.5	1.6	1.9	0.5	0.0	9.4	0.7	1.64	7.69	Zr_7Ni_{10}
Cu4-2	**11.2**	**20.1**	**12.5**	**30.6**	**4.3**	**9.8**	**8.6**	**0.4**	**2.3**	**0.2**	**2.19**	**6.82**	**AB_2**
Cu4-3	3.5	86.2	2.5	3.9	0.2	1.4	1.0	0.0	0.1	1.2	0.11	4.46	ZrO_2
Cu4-4	19.8	17.7	1.5	46.0	2.3	2.5	0.4	0.2	8.8	0.8	1.67	7.67	TiNi
Cu5-1	15.9	22.4	0.7	47.1	0.9	1.3	0.2	0.3	10.7	0.5	1.61	7.72	Zr_7Ni_{10}
Cu5-2	16.6	21.3	1.1	45.6	0.9	1.9	0.4	0.3	11.2	0.7	1.64	7.71	Zr_7Ni_{10}
Cu5-3	**11.0**	**20.0**	**14.0**	**26.2**	**3.3**	**10.8**	**11.6**	**0.2**	**2.7**	**0.2**	**2.23**	**6.62**	**AB_2**
Cu5-4	3.5	82.5	3.2	6.1	0.3	1.8	1.8	0.0	0.4	0.4	0.16	4.57	ZrO_2

level in Fig. 2. The small gray area is identified as the TiNi phase. TiNi is observed in every sample except Cu5. The amount of TiNi phase decreases with the increase in Cu-content. In general, as the Cu-content increases, the secondary phase shifts from TiNi to Zr_7Ni_{10}.

In Fig. 5, the Zr and Ti-contents in the Zr_7Ni_{10} phase are plotted as functions of Cu-content. As the Cu-content increases, there is a trend of decreasing Zr-content in the Zr_7Ni_{10} phase while Ti-content remains relatively unchanged. The effect of reduced Zr-content to the lattice size is two-fold: reduction in the average A-site atom size and reduction in the A-to-B stoichiometric ratio. The net result exceeds that from the relatively larger Cu replacing the smaller Co and contributes to a shrinking unit cell as can be seen from the peak shift in the XRD patterns in Fig. 1.

3.3. Gaseous phase study

The gaseous phase hydrogen storage properties of the alloys were studied by PCT. The resulting absorption and desorption isotherms measured at 30 and 60 °C are shown in Fig. 6. The information obtained from the PCT study is summarized in Table 5. The equilibrium plateau pressure, defined as the mid-point of the desorption isotherm, decreases with the increase in Cu-content and agrees with the expanding C14 unit cell. The slope factor (SF) is defined as the ratio of the storage capacity between 0.01 and 0.5 MPa to the total capacity. The SF of each alloy is listed in Table 5 and can be used to predict the degree of disorder in the alloy [36,37]. As the Cu-content increases, the SF decreases monotonically, which indicates that the degree of disorder increases. This result agrees, in general, with the smaller crystallite sizes in higher Cu-content alloys found by XRD analysis. The hysteresis of the PCT isotherm, listed in Table 5, is defined as $\ln(P_a/P_d)$, where P_a and P_d are the absorption and desorption equilibrium pressures at the mid-point, respectively. The hysteresis can be used to predict the pulverization rate of the alloy during cycling [27–29]. In this case, hysteresis increases with the increase in Cu-content, which agrees with the decreasing a/c ratio according to the correlation established previously [27–29]. Alloys with higher Cu-content are more prone to pulverization during cycling, and this observation is coincidentally the same as in the case of Cu-addition to AB_5 alloys [38]. The poor cycle performance with Cu-incorporation in AB_2 alloy has also been validated before [14].

In the annealed alloy, some contradictory results of Cu-incorporation in the TiZrCrMn AB_2 alloy were previously reported [11]: SF was reduced due to a reduction in the strain effect, and PCT isotherm hysteresis was lowered. The main difference between

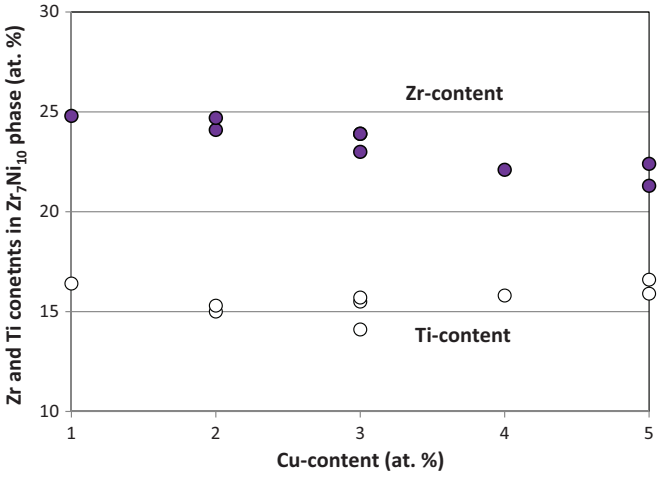

Fig. 5. Zr and Ti-contents in the Zr_7Ni_{10} secondary phase as functions of Cu-content.

Table 5
Summary of gaseous phase properties (plateau pressure, slope factor, hysteresis, maximum and reversible capacities, and changes in enthalpy and entropy) and results from half-cell measurement (capacities at the 10th cycle, high-rate dischargeability at the 10th cycle, cycles needed to achieve 80% of maximum HRD, bulk diffusion coefficient, surface exchange current, and −40 °C charge transfer resistance and double-layer capacitance).

Des.	Des. pressure @ 30 °C (MPa)	SF @ 30 °C (%)	PCT hysteresis @ 30 °C	Max. cap. @ 30 °C (wt.%)	Reversible cap. @ 30 °C (wt.%)	$-\Delta H$ (kJ mol^{-1})	$-\Delta S$ (J mol^{-1} K)	Cap. @ 50 mA g^{-1} (mAh g^{-1})	Cap. @ 4 mA g^{-1} (mAh g^{-1})	HRD	Activation cycle #	Cycle reaching 70% cap. @ 4 mA	D (10^{-10} cm^2 s^{-1})	I_0 (mA g^{-1})	Charge transfer resistance @ −40 °C (Ω g)	Double-layer capacitance @ −40 °C (F g^{-1})
Cu0	0.056	81	0.08	1.49	1.38	34.8	110	346	366	0.94	6	135	2.5	22.5	70	0.12
Cu1	0.056	82	0.22	1.39	1.21	29.8	94	354	385	0.92	4	115	1.5	20.1	48	0.19
Cu2	0.042	80	0.23	1.30	1.15	31.4	97	358	386	0.93	4	98	1.6	28.4	79	0.26
Cu3	0.031	74	0.44	1.20	0.94	31.7	95	350	382	0.92	2	95	1.1	22.2	59	0.28
Cu4	0.029	74	0.57	1.14	0.90	32.1	96	349	378	0.92	4	102	1.2	19.0	101	0.23
Cu5	0.029	69	0.37	1.11	0.86	31.5	93	280	352	0.80	11	167	1.1	9.5	197	0.31

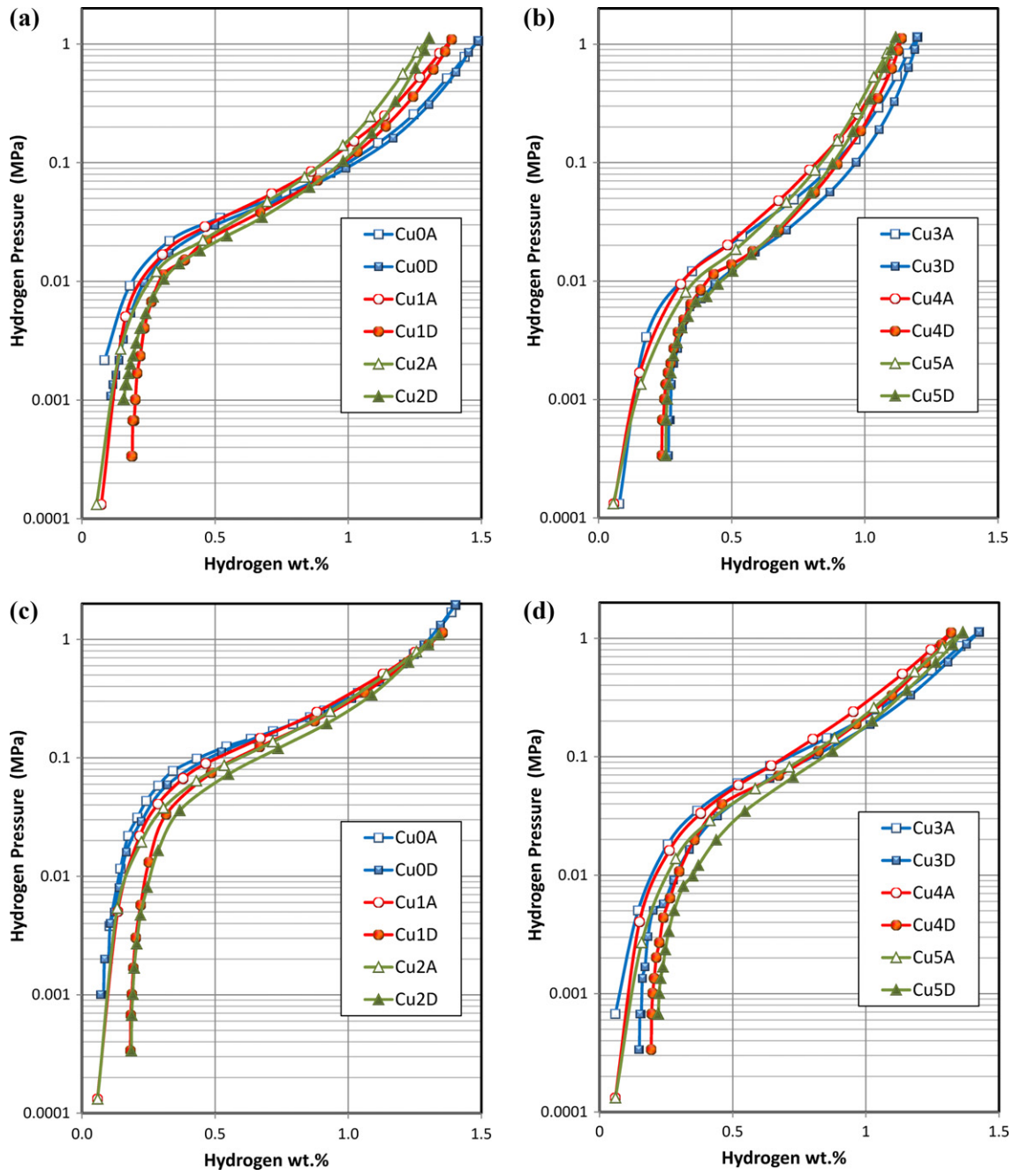

Fig. 6. PCT isotherms of alloys Cu0, Cu1, and Cu2 measured at 30 °C (a) and 60 °C (c), and Cu3, Cu4, and Cu5 measured at 30 °C (b) and 60 °C (d). Open and solid symbols are for absorption and desorption curves, respectively.

unannealed and annealed samples is the existence of the secondary phase. The secondary phase in the current study prevents the completion of the ordered metal hydride structure and yields a lower storage capacity when compared to the annealed sample. Evidently, the additional Cu has different effects to the PCT characteristics depending whether the final metal hydrogenation is completed or not.

As Cu-content increases, both the 30 °C maximum and reversible hydrogen storage capacities decrease, as seen from data listed in Table 5. The room temperature storage capacity reduces with an increase in V_{C14}, which is seldom observed in MH alloys. With the increase in Cu-content, the abundance of Zr_7Ni_{10}, known for its detrimental effect to the gaseous phase storage capacity [24], increases and reduces both capacities. In this case, the effect of the secondary phase is larger than that of the main phase.

Desorption equilibrium pressure at mid-point measured at 30 and 60 °C were used to calculate the changes in enthalpy (ΔH) and entropy (ΔS) by the equation

$$\Delta G = \Delta H - T\Delta S = RT \ln P \quad (1)$$

where R is the ideal gas constant and T is the absolute temperature. The results of these calculations are listed in Table 5. The ΔH and ΔS values are similar among the Cu-containing alloys and are higher than those of the Cu-free Cu0 alloy. According to the linear dependency between ΔH and V_{C14} discovered by Nakano et al. [39], the difference in V_{C14} between Cu0 and Cu5 should contribute to a decrease in ΔH of 4.2 kJ mol^{-1} H_2. However, the experimental data show an increase of 3.3 kJ mol^{-1} H_2 instead. Judging from the fact that ΔS values of the Cu-containing alloys are significantly higher than those of AB_2 MH alloys [20,21,40], it is possible that the

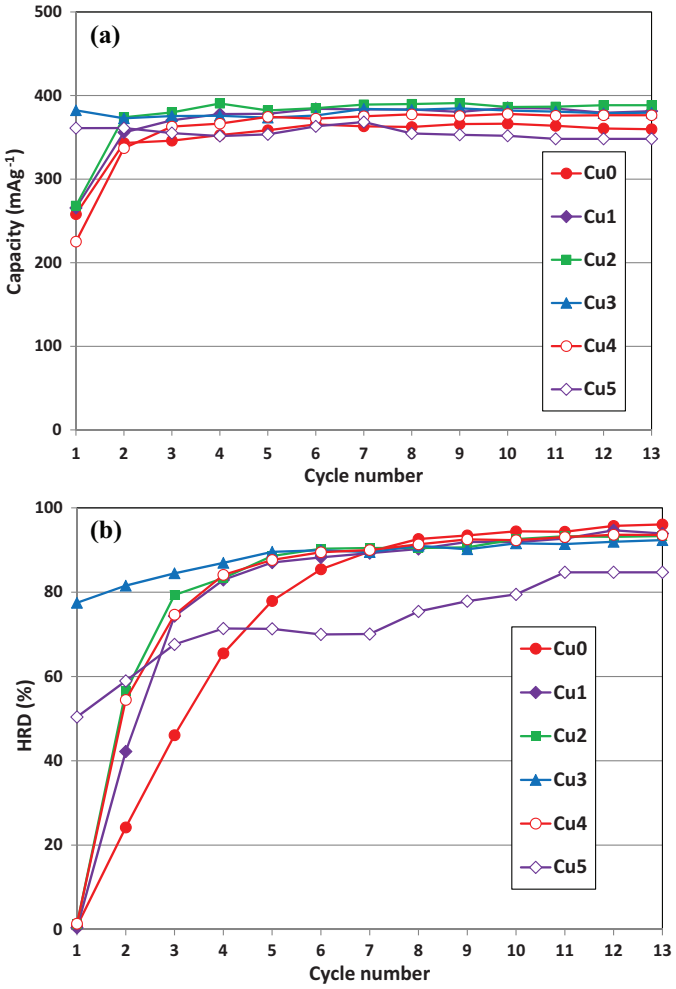

Fig. 7. The half-cell discharge capacity measured at 4 mA g^{-1} (a) and high-rate dischargeability (HRD) and (b) of the first 13 cycles.

filling of an ordered MH structure is not completed. Therefore, the reduction of gaseous phase storage capacity of C14 main phase is due to the detrimental effect from the neighboring Zr_7Ni_{10} phase that causes an incompletion in the formation of a complete ordered metal hydride structure.

3.4. Electrochemical measurement

The discharge capacity of each alloy was measured in a flooded-cell configuration against a partially pre-charged $Ni(OH)_2$ positive electrode. No alkaline pretreatment was applied before the half-cell measurement. Each sample electrode was charged at a constant current density of 50 mA g^{-1} for 10 h and then discharged at a current density of 50 mA g^{-1} followed by two pulls at 12 and 4 mA g^{-1}. The obtained full capacities (4 mA g^{-1}) from the first 13 cycles are plotted in Fig. 7a. Cu3 and Cu5 reach the stabilized full capacity at the first cycle while the other samples take one more cycle to do so. High-rate (50 mA g^{-1}) and full capacities (4 mA g^{-1}) measured at the 10th cycle are listed in Table 5. As the Cu-content increases in the alloy, both capacities first increase and then decrease. Alloy Cu2 has the highest of both capacities. The electrochemical capacity results do not agree with those measured in gaseous phase because the poisoning from Zr_7Ni_{10} secondary phase in the gaseous phase storage capacity is more severe than it is in the electrochemical environment.

The half-cell HRD of each alloy, defined as the ratio of discharge capacity measured at 50 mA g^{-1} to that measured at 4 mA g^{-1}, for the first thirteen cycles are plotted in Fig. 7b. It takes more cycles to reach a stabilized HRD value when compared to achieving the full capacity. While the activation for the capacity requires creating a surface oxide capable of splitting and recombining water molecules, the activation for the HRD requires forming a stabilized surface area through the initial powder pulverization. The cycle number needed to reach 80% of the stabilized HRD value for each alloy is listed in Table 5. As more Cu is added in the alloy formula, pulverization becomes easier in the beginning, which agrees with the decreasing a/c ratio and the increasing PCT hysteresis. As the Cu-content further increases, the abundance of Zr_7Ni_{10} phase increases. Zr_7Ni_{10} has been shown to have a low pulverization rate when compared to that of C14 [34] and thus increases the number of activation cycles.

The end of a battery's cycle life was defined as when the low-rate capacity (4 mA g^{-1}) reaches 70% of its original value; cycle life values are also listed in Table 5. The trend of half-cell cycle life is similar to that of activation cycle. As the Cu-amount increased in the beginning, the cycle life was decreased due to the higher pulverization rate from the larger PCT hysteresis. The cycle life was then improved due to the combination of the higher Zr_7Ni_{10} phase abundance and the lower storage capacity (less volume expansion during hydriding). The HRD values from the tenth cycle are listed in Table 5. Except for Cu5, the HRD values of the Cu-containing alloys are similar and slightly lower than the Cu-free base alloy Cu0. In a previous study of effects from various secondary phases, TiNi impedes while Zr_7Ni_{10} improves the HRD performance [24]. However, the improvement in HRD from increasing Zr_7Ni_{10} phase abundance was not observed in this study. Factors other than the synergetic effect from secondary phase dominate the electrochemical properties in the Cu-modified alloys.

In order to further understand the source of the degradation in HRD of the Cu-containing alloys, both the bulk diffusion coefficient (D) and the surface exchange current (I_o) were measured. The details of both parameters' measurements were reported previously [41], and the values are listed in Table 5. The D values from the Cu-containing alloys are about half of that of the Cu-free Cu0 alloy. Since Zr_7Ni_{10} was reported to contribute positively to the HRD value, Cu in the main C14 phase is responsible for the relatively slow diffusion of hydrogen, which may be related to the stronger metal–hydrogen bond due to the larger V_{C14} and lower plateau pressure. The I_o values of Cu-free and Cu-containing alloys are similar except for Cu5, which implies that Cu only slightly modifies the surface oxide. However, this observation is very different from the case of Cu-modifying AB_5 alloys [4–6]. In conclusion, the reason of the Cu-containing alloys' lowers HRD values is mainly the formation of a relatively more stable hydride that contributes to slower hydrogen diffusion in the bulk.

The low-temperature characteristics were further studied by the AC impedance measurement conducted at −40 °C. The charge-transfer resistance and double-layer capacitance of each alloy were calculated from the Cole–Cole plot and are listed in Table 5. The capacitances, which are closely related to the surface area, of the Cu-containing alloys are higher than that of the Cu-free alloy and indicate a positive contribution of Cu to the increase in surface area (due to the higher pulverization rate). The resistance measured at −40 °C first decreases and then increases with the increase in Cu-content. In most of the MH alloy systems observed so far, the increase in surface area usually results in a lower surface charge transfer resistance [21,42,43]. In the current study, as the Cu-amount increases, both the surface area and surface charge transfer resistance increased. The presence and increase in the amount of

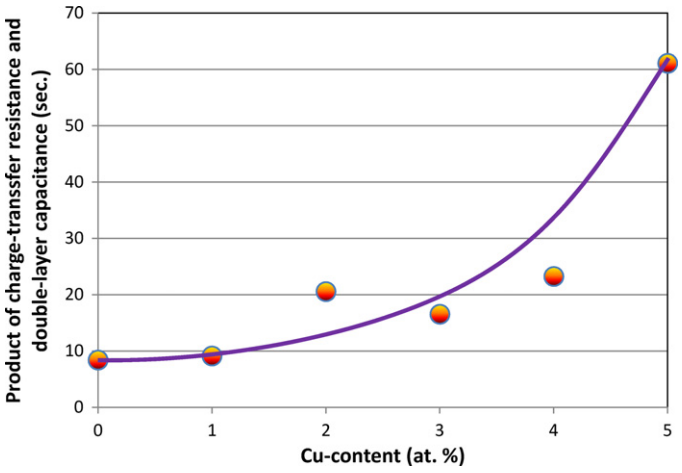

Fig. 8. The product of charge-transfer resistance and double-layer capacitance measured at −40 °C as a function of Cu-content.

Zr_7Ni_{10} minor phase possible explain the dramatic degradation in the surface catalytic activity overshadowing the increase in the surface area. This finding also agrees with the HRD measured at room temperature. Furthermore, the product of charge-transfer resistance and double-layer capacitance was plotted against Cu-content in Fig. 8. This product removes the contribution of the surface area and remains constant in the beginning of Cu-content increase. It then exponentially increases at higher Cu-content. This result suggests that Cu > 1 at.% has a detrimental effect on the low-temperature performance of AB_2 MH alloys.

4. Summary

The structure, gaseous phase, and electrochemical properties of a series of Cu-modified AB_2 alloys ($Ti_{12}Zr_{21.5}V_{10}Cr_{7.5}Mn_{8.1}Co_{8.0-x}Ni_{32.2}Cu_xSn_{0.3}Al_{0.4}$, $x = 0$ to 5) were studied. As the Cu-content in the alloys increases, the following changes occur: the secondary phase shifts from TiNi to Zr_7Ni_{10}; the C14 unit cell expands and forms a more stable hydride which lowers the equilibrium pressure, improves the electrochemical capacities, reduces the bulk hydrogen diffusion coefficient; the HRD deteriorates; and a/c ratio decreases (which corresponds well with the increase in PCT hysteresis) – as a result, the higher pulverization rate which facilitates the formation process is observed. The increase in Zr_7Ni_{10} reduces the gaseous phase hydrogen storage capacity and prevents the completion of ordered metal hydride formation in the C14 main phase. Although incorporation of Cu increases the surface area, the surface charge-transfer resistance at −40 °C increases after Cu > 1 at.%. In summary, Cu-addition trades HRD for higher capacity and easier formation at room temperature, and 1 at.% of Cu is suggested for low-temperature applications.

References

[1] S.R. Ovshinsky, M.A. Fetcenko, J. Ross, Science 260 (1993) 176.
[2] M.A. Fetcenko, S.R. Ovshinsky, K. Young, B. Reichman, C. Fierro, J. Koch, F. Martin, W. Mays, T. Ouchi, B. Sommers, A. Zallen, J. Alloys Compd. 330–332 (2002) 752.
[3] M.A. Fetcenko, S.R. Ovshinsky, B. Reichman, K. Young, C. Fierro, J. Koch, A. Zallen, W. Mays, T. Ouchi, J. Power Sources 165 (2007) 544.
[4] M.A. Fetcenko, S.R. Ovshinsky, K. Young, B. Reichman, T. Ouchi, J. Koch, W. Mays, U.S. Patent 6,830,725 (2004).
[5] K. Young, T. Ouchi, M.A. Fetcenko, U.S. Patent 7,344,677 (2008).
[6] K. Young, T. Ouchi, A. Banik, J. Koch, M.A. Fetcenko, L.A. Bendersky, K. Wang, J. Alloys Compd. 509 (2011) 4896.
[7] A. Drašner, Ž. Blažina, J. Less Common Met. 175 (1991) 103.
[8] B. Liu, D. Kim, K. Lee, J. Lee, J. Alloys Compd. 240 (1996) 214.
[9] K. Oguro, M. Tanaka, U.S. Patent 5,100,615 (1992).
[10] B.K. Singh, S. Cho, H. Yoon, C. Kim, K.S. Bartwal, Mater. Chem. Phys. 112 (2008) 686.
[11] J. Park, H. Jang, S. Han, P. Lee, J. Lee, J. Alloys Compd. 325 (2001) 293.
[12] Y. Yamamura, H. Seri, Y. Tsuji, N. Owada, T. Iwaki, U.S. Patent 5,532,076 (1996).
[13] Y. Izumi, Y. Moriwaki, K. Yamashita, T. Tokuhiro, U.S. Patent 5,962,156 (1999).
[14] S. Han, M. Zhao, L. Wu, Y. Zheng, Chem. J. Chin. Univ. 24 (2003) 2256.
[15] A. Züttel, F. Meli, L. Schlapbach, J. Alloys Compd. 206 (1994) 31.
[16] D. Kim, H. Lee, K. Cho, J. Lee, J. Alloys Compd. 282 (1999) 261.
[17] B. Hariprakash, S.K. Martha, A.K. Shukla, J. Appl. Electrochem. 33 (2003) 497.
[18] K. Young, M.A. Fetcenko, T. Ouchi, F. Li, J. Koch, J. Alloys Compd. 464 (2008) 238.
[19] K. Young, M.A. Fetcenko, J. Koch, K. Morii, T. Shimizu, J. Alloys Compd. 486 (2009) 559.
[20] K. Young, T. Ouchi, B. Huang, B. Reichman, M.A. Fetcenko, Int. J. Hydrogen Energy (2011), doi:10.1016/j.ijhydene.2011.06.117.
[21] K. Young, T. Ouchi, B. Huang, B. Reichman, M.A. Fetcenko, J. Power Sources 196 (2011) 8815.
[22] Z. Shi, S. Chumbley, F.C. Laabs, J. Alloys Compd. 312 (2000) 41.
[23] J.H. Zhu, P.K. Liaw, C.T. Liu, Mater. Sci. Eng. A239–240 (1997) 260.
[24] K. Young, J. Nei, T. Ouchi, M.A. Fetcenko, J. Alloys Compd. 509 (2011) 2277.
[25] W.J. Boettinger, D.E. Newbury, K. Wang, L.A. Bendersky, C. Chiu, U.R. Kattner, K. Young, B. Chao, Metall. Mater. Trans. A 41 (2010) 2033.
[26] L.A. Bendersky, K. Wang, W.J. Boettinger, D.E. Newbury, K. Young, B. Chao, Metall. Mater. Trans. A 41 (2010) 1891.
[27] K. Young, T. Ouchi, M.A. Fetcenko, J. Alloys Compd. 480 (2009) 428.
[28] K. Young, T. Ouchi, W. Mays, B. Reichman, M.A. Fetcenko, J. Alloys Compd. 480 (2009) 434.
[29] K. Young, T. Ouchi, M.A. Fetcenko, J. Alloys Compd. 480 (2009) 440.
[30] H.P. Klug, L.E. Alexander, X-ray Diffraction Procedures for Polycrystalline and Amorphous Materials, 2nd ed., John Wiley & Sons, New York, 1974, p. 656.
[31] K. Young, T. Ouchi, B. Huang, J. Nei, M.A. Fetcenko, J. Alloys Compd. 501 (2010) 236.
[32] H.T. Takeshita, N. Fujiwara, T. Oishi, D. Noréus, N. Takeichi, N. Kuriyama, J. Alloys Compd. 360 (2003) 250.
[33] H.T. Takeshita, S. Kondo, H. Miyamura, N. Takeichi, N. Kuriyama, T. Oishi, J. Alloys Compd. 376 (2004) 268.
[34] K. Young, T. Ouchi, Y. Liu, B. Reichman, W. Mays, M.A. Fetcenko, J. Alloys Compd. 480 (2009) 521.
[35] K. Young, T. Ouchi, M.A. Fetcenko, W. Mays, B. Reichman, Int. J. Hydrogen Energy 34 (2009) 8695.
[36] K. Young, T. Ouchi, J. Koch, M.A. Fetcenko, J. Alloys Compd. 477 (2009) 749.
[37] K. Young, T. Ouchi, M.A. Fetcenko, R.K. Regmi, G. Lawes, J. Alloys Compd. 490 (2010) 282.
[38] Y. Osumi, H. Suzuki, A. Kato, K. Oguro, S. Kawai, M. Kaneko, J. Less Common Met. 89 (1983) 287.
[39] H. Nakano, S. Wakao, T. Shimizu, J. Alloys Compd. 253–254 (1997) 609.
[40] K. Young, M.A. Fetcenko, F. Li, T. Ouchi, J. Koch, J. Alloys Compd. 468 (2009) 482.
[41] F. Li, K. Young, T. Ouchi, M.A. Fetcenko, J. Alloys Compd. 471 (2009) 371.
[42] K. Young, T. Ouchi, B. Reichman, J. Koch, M.A. Fetcenko, J. Alloys Compd. 509 (2011) 3995.
[43] K. Young, T. Ouchi, B. Reichman, J. Koch, M.A. Fetcenko, J. Alloys Compd. 509 (2011) 7611.